RSC Advances

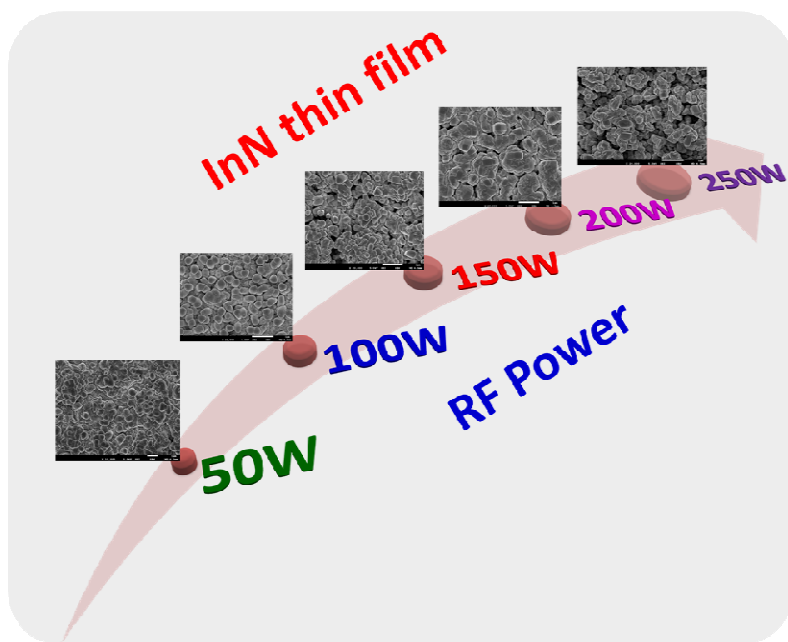# Investigation on the electrochemical behavior of indium nitride thin films by plasma assisted reactive evaporation

SCHOLARONE™
Manuscripts

Investigation on the electrochemical behaviour of indium nitride thin films by plasma-assisted reactive evaporation

Graphical Abstract

Indium nitride thin films were grown at different RF power by plasma-assisted reactive evaporation method and their electrochemical properites were investigated.

Investigation on the electrochemical behavior of indium nitride thin films by plasma-assisted reactive evaporation

Vattikondala Ganesh[*], **Mahdi Alizadeh**[*], **Ahamad Shuhaimi, Alagarsamy Pandikumar, Goh Boon Tong , Nay Ming Huang and Saadah Abdul Rahman**

Low Dimensional Materials Research Centre, Department of Physics, Faculty of Science, University of Malaya, 50603 Kuala Lumpur, Malaysia.

Corresponding authors: 1. Vattikondala Ganesh, e.mail: 80.vganesh@gmail.com*, Tel: +601114310910. 2. Mahdi Alizadeh, *e.mail: alizadeh_kozerash@yahoo.com*, Tel: +60123290697.

Abstract

Indium nitride (InN) thin films were deposited on Si (111) substrate by plasma-assisted reactive evaporation with different radio frequency (RF) power supply. The effect of RF power on the structural, morphological, and optical properties of the films were investigated by X-ray diffraction analysis, scanning electron microscope, energy-dispersive X-ray analysis, UV-Vis transmittance, and micro Raman spectroscopy. The electrochemical behavior of the InN thin films were investigated in 0.1 M KOH electrolyte towards electrochemical water splitting. Linear sweep voltammograms revealed that the anodic current decreases by increasing RF power for the growth of InN thin films. The charge transfer dynamics between the InN thin film and electrolyte interfaces during the electrochemical process were studied using electrochemical impedance spectroscopy (EIS). Variations in Donor density and flat band potentials of InN thin films were deduced from the Mott–Schottky plots. Further, the electrocatalytic behavior of InN thin films was investigated with a $K_3[Fe(CN)_6]$ redox probe. The good electrochemical behavior of InN thin films showed that this material could be a potential candidate for water splitting application.

Keywords: Indium Nitride, Plasma-assisted reactive evaporation, Thin film, Electrochemical Properties.

1.   Introduction

In the last decades, the group III-nitrides (III-Ns) have emerged as the pre-eminent universal materials for the science and technology of compound semiconductors. This is due to their superior physical properties which can be employed in many optoelectronic, nanoelectronic and opto-chemical devices [1-4]. Among the III-Ns, indium nitride (InN) has attracted increasing scientific and commercial attention owing to its excellent properties such as high electron mobility, low effective mass for free electrons and high saturation velocity which make it suitable for high speed electronic devices [5]. In addition, InN has received considerable interest for the development of chemical sensors and biosensors because of its high surface donor density and the corresponding compensation surface electron accumulation, chemical inertness, and chemical recognition capabilities [6-10].

The electrochemical (EC) and photoelectrochemical (PEC) properties of III-N semiconductor for water splitting have been proved, recently [11-14]. B AlOtaibi *et al.* [11] explored the PEC behavior of GaN nanowires and found that not only the arrays can function as highly efficient PEC photoactive electrodes, but also the PEC properties can be effectively controlled by dopant incorporation in the electrode. High performance of water splitting by GaN and hybrid NiO/GaN photoanodes were reported by S.H. Kim *et al.* [12]. J Wallys *et al.* [13] obtained high surface capacitance and low surface resistance from the electrochemical characteristics of Si-doped GaN nanowires. However, less work about both EC and PEC properties of InN films have been reported so far. It is may be due to the fact that the band-gap energy of InN is now considered to be 0.7 eV [15], not the previously accepted value of 1.9 eV. The possible reason for the high band-gap value are the Moss-Burstein (MB) shift, presence of oxygen impurity, and other stoichiometry-related defects [16-21]. It has been shown that materials with band-gap energy value of ~2.0 eV exhibits higher

efficiency for PEC water splitting [22]. Hence, unintentional presence of oxygen in the InN thin films with bandgap energy ~2.0 eV could be a competitive candidate for water splitting.

InN thin-films have been deposited on different substrates such as sapphire, glass and Si by various methods including plasma-assisted molecular beam of epitaxy (PA-MBE) [23], metal organic chemical vapor deposition (MOCVD) [24], Pulsed laser deposition (PLD) [25] and reactive d.c. magnetron sputtering [26]. Although MOCVD is a well-stablished method in terms of device production, high decomposition temperature is required in the process for ammonia decomposition which has disadvantages of degradation of the substrate and film deterioration due to thermal stresses [27]. Also, this method is restricted by type of substrate since only specified substrates such as sapphire and GaN can be used for deposition. The properties of crystalline thin films grown using a PLD system are undesirably affected by the repetition frequency of the applied laser pulses [28]. Moreover, the growth rate of sputtering-based processes is quite low, though the deposited films are highly crystalline.

The present work describes the electrochemical properties of InN thin films deposited on a Si (111) substrate by plasma-assisted reactive evaporation method. One of the most substantial advantages of plasma-assisted reactive evaporation is the high deposition rate which is favorable for low cost production. The hot filament, as the evaporation tool, can also effectively dissociate N_2 molecules and gives rise to the generated In and N species gaining enough kinetic energy when they travel towards the substrate surface [29]. Upon hitting the surface, thermal energy of the energized neutral species is released onto the top-most layers of substrate surface providing an internal heating channel [30, 31]. Plasma is a suitable medium for the generation of growth species, activation of surface bonds and post-processing of nanomaterials [32-34]. In addition, a plasma discharge can effectively control the generation, transport, and deposition of growth building units (BU) on an

exposed-substrate surface [32-35]. The role of plasma ambient becomes much more crucial by considering the fact that the properties of plasma-aided-deposited thin films can be affected by the plasma parameters such as the applied radio frequency (RF) power [35]. Therefore, plasma assisted reactive evaporation, as a technique that encompasses all notions of hot-filament-led BU generation, plasma-enabled BU generation could be a promising approach for energy-efficient deposition of InN thin films. Moreover, preparation of thin films by the proposed method at relatively low substrate temperatures simplifies deposition system, shortens time of the process and as a result makes it possible to gain higher throughout at low cost.

2. Experimental Method

2.1. Growth of InN Thin films

Homemade plasma-assisted reactive evaporation system was employed for the growth of InN thin films on a Si (111) substrate. A schematic diagram of the system is shown in fig.1. The stainless steel reactor consists of two parallel electrodes. The upper electrode served as a gas showerhead and was connected to RF power of 13.56 MHz coupled with matching analyzer. The substrate holder was used as the lower electrode and was grounded. The distance between the upper and grounded electrodes was 4.5 cm. A tungsten wire was used as a filament and fixed at 1 cm above the substrate holder. Prior to deposition, the Si Substrate was cleaned ultrasonically with acetone and isopropanol for a period of 10 min followed by rinsing with deionized water. The native oxide layer was removed from the Si substrate by acid cleaning (aqueous solution of HCL, NH_4OH, and HF) before loading into the chamber. Indium wire with 99.999% purity was placed inside the tungsten filament. The reactor chamber was pumped down to a background pressure of 3.5×10^{-5} mbar. A constant substrate temperature was maintained at 350 °C during the deposition using a rod type heater placed under the

4

substrate holder. Hydrogen (H_2) plasma treatment was performed on the substrate surface prior to actual deposition. InN thin films were deposited at constant N_2 flow rate of 80 sccm with different RF powers (50, 100, 150, 200 and 250 W) for 5 min. A post annealing treatment was performed in N_2 ambient at 50 W for 30 min after deposition in the same chamber.

2.2. Characterization of InN thin films

The crystalline nature and structural properties of the samples were characterized using X-ray diffraction (XRD) by SIEMENS D5000 X-ray diffractometer (Cu Kα X-ray radiation λ = 1.54060 Å) and micro-Raman spectrometer (Renishaw Raman microscope) using a laser source of Ar^+ with a selected excitation wavelength of 514.5 nm. The surface morphology and elemental composition of the samples were examined by field emission scanning electron microscopy (FESEM, FEI Quanta 200) intergraded with energy-dispersive X-ray spectroscopy (EDX) accessory. Optical studies were examined by UV-Vis-Infrared spectrophotometer (Lambda 750, PerkinElmer). The thickness of the films was measured using surface profiler (KLA-Tencor).

2.3 Electrochemical analysis of InN thin films

The electrochemical behaviors of the grown InN thin films at different RF power were studied using a computer-controlled VersaSTAT 4 Electrochemical Workstation (Princeton Applied Research, USA). The I-V, EIS, and Mott–Schottky characterization have been carried out in the presence of 0.1 M KOH using the InN, Ag/AgCl, and Pt electrodes as a working, reference, and counter electrodes, respectively. The cyclic voltammogram for different InN thin films was recorded in the presence of 1 mM $K_3[Fe(CN)_6]$ and 0.1 M KCl at a scan rate of 50 mV/s. In the present investigation, the working electrode potential stated was measured against the reference electrode, Ag/AgCl. All electrochemical measurements were carried out at room temperature.

3. Results and discussions

Figure 2 shows the XRD patterns of InN samples prepared at different RF powers (50–250 W). Five major peaks are observed from XRD pattern of the InN films deposited RF power of 50 W. The peaks centered at 2θ= 30.50°, 35.40°, 50.90° and 60.70° are assigned to (222), (400), (440) and (622) planes of cubic indium oxide, respectively [36]. The peak appeared at 2θ= 33° is corresponded to (101) plane of InN. It clearly indicates the existence of nitride and oxide phases in the InN film deposited RF power of 50 W. The XRD pattern the samples deposited at the RF powers of 100, 150, 200 and 250 W shows diffraction peaks at 2θ = 29.10°, 31.15°, 33°, 43°, 52°, 56.65°, 61.45° and 62.60° which are corresponded to (100), (002), (101), (102), (110), (103), (112) and (201) planes of wurtzite InN, respectively. The peak positions are in agreement with the existing literature [37-39] and the corresponding miller indexes were marked near the peaks. The strongest peak, (101), corresponds to hexagonal InN, hence it can be concluded that the majority of the films are hexagonal InN. As RF power increases, the (101) plane intensity first increases and reaches a maximum at 200 W. Then it decreases which may be due to enhanced re-sputtering rates at high RF power. Therefore, the RF power should not be as high as the re-sputtering rate exceeds the growth rate. The high intensity of the diffraction peaks for the film deposited at 200 W indicates higher crystallinity.

Figure 3 shows the micro Raman spectrum of InN thin films deposited at various RF powers in the spectrum range of 100-900 cm^{-1}. Probe depth of the Raman spectrometer utilized for characterization of the grown films was 257 nm. For all the measurements, the laser's beam incidence is normal to the surface. InN has a wurtzite structure and belongs to C^4_{6v} space group. The micro-Raman spectra of all the films deposited at various RF powers reveal a broad peak observed between 170–215 cm^{-1} with a center maximum of 190 cm^{-1} which is assigned to B_2 (low) phonon mode of InN

6

[40,41]. This region is dominated by the overtones of acoustic phonon modes. In addition, For all samples the Raman spectra show one major peak (at around 570 cm^{-1}) and one shoulder (at around 490 cm^{-1}) which are corresponded to $A_1(LO)$ and $E_2(high)$ phonon modes of InN, respectively [40,41]. E_2 (High) and A_1 (LO) bands show broadening and almost merge into a singlewide band to suggest the presence of an amorphous state with short-range order. It has been shown that for the samples grown at less than 400 °C, the structure disorder and sample roughness become more pronounced [41]. The Raman spectra of all samples are very similar, although the XRD spectrum of the sample deposited at 50W is quite different from others. This inconsistency can be explained by taking into account vibrational phonon modes of cubic indium oxide. In-O phonon vibration mode (as a characteristic of cubic In_2O_3) is also at around 490 cm^{-1} [42]. Therefore, the observed shoulder at around 490 cm^{-1} in the Raman spectrum of the films deposited at 50 W is possibly due to overlapping of In-O phonon vibration and InN $E_2(high)$ modes.

The FESEM results strongly indicate that the surfaces of the all InN films are very rough. FESEM and EDX results of InN thin films deposited on Si (111) substrate are shown in **Figure 4(a-f).** FESEM results of all the samples showed agglomeration of InN nanoparticles resulting in formation of excessively large grains. The film deposited at 50 W (**figure 4(a)**) shows a cauliflower-like morphology of grains with size of 300-600 nm. The density of agglomeration is high due to low surface temperature at low RF power, which leads to less kinetic energy of adatoms. Adatoms tend to agglomerate before they find a suitable site for growth because of low kinetic energy. As RF power increases, the films still show agglomeration features but the compactness or density of agglomeration is less than the sample prepared at 50 W due to an increase of surface temperature, which leads to increases in kinetic energy of adatoms. The surface morphology of InN thin film prepared at 100 W (**figure 4(b)**) shows formation of grains with uniform size (~300-400 nm) and

shape, whereas the sample prepared at above 100W i.e. 150, 200, and 250 W images show clear hexagonal faceted morphology and the size of the crystal increases up to 200 W. The grain size in the films deposited at 150 W (**figure 4(c)**) is in the range of 200-300 nm. Due to increase of surface temperature as a results of ion bombardment from plasma environment, the agglomeration effect is enhanced for the sample grown at RF power of 200 W (**figure 4(d)**) which results in larger grains with size of 500 – 1000 nm W. However, further increase of RF power to 250 W (**figure 4(e)**) causes to re-sputtering of the films and the grain size decreases to around 300-500 nm. This is also supported by XRD results shows that the crystallinity of the films prepared at RF power of higher than 200 W decreases. **Figure 4(f)** shows the elemental composition of the all samples determined from the EDX analysis. It should be noticed that EDX does not sufficiently provide accurate information on elemental composition and quality of thin films. However, this measurement tool was employed to compare the elemental content of the films at various growth conditions. All the samples have In, N, and O, the atomic concentration of N and O are greatly affected with respect to RF power. As the RF power increases, the atomic percentage of N increases, whereas O percentage reduces. The oxygen concentration in the samples is relatively high and it has been reported that the oxygen mainly resides at the grain boundaries or on the surface [43]. The increase of RF power leads to dissociation of N_2 molecules more effectively and not only favors the growth of InN but also reduction of oxygen contamination in the grown films. As a matter of fact this method provides control of nitrogen species by controlling the plasma power. Since the N^+ ions are accelerated by the electric field in the plasma ambient, by increasing the RF power from 50 to 200 W, the energy of the ions striking the substrate is enhanced, significantly. Therefore, the higher mobility of nitrogen adatoms on the substrate surface ensures that the N adatoms reach to the all deposited indium metal and get reacted. As a result, less free bonds of the metallic adatoms are left for O contamination and oxygen content in the films

decreases. K.P. Biju, M.K. Jain [44] employed the similar method for growth of InN films and reported that when substrate is biased by RF voltage of a cathode connected to the substrate, the nitrogen content of the films increases. A further increase of RF power to 250 W slightly increases the oxygen concentrations due to the re-sputtering effect. The possible reason is dissociation of InN into In and N atoms due to an increase in surface temperature and thereby oxidation of In surface.

In order to obtain direct optical bandgap of the InN films, the deposition was performed on quartz substrates. **Figure 5** displays the squared absorption coefficient $(\alpha)^2$ of the all films as a function of photon energy ($h\upsilon$). The absorption coefficient was calculated using transmission and reflectance data as well as the thickness of the films. The value of the optical bandgap is determined by extrapolating the linear part of the curve to energy axis in **Figure 5**.The tailing effect shows fairly well in linear form for all the samples except the sample deposited at 50 W, indicate that the allowed direct transition in InN. The tailing effect observed at 50 W is not well fitted because of the presence of InN and In_2O_3 phases. The thickness and obtained bandgap energy of each sample are provided in table 1. The optical bandgap energy (E_g) of the films deposited at 100, 150, 200, 250 W are 1.80, 2.00, 2.00 and 1.95 eV, respectively. These values are very close to the E_g of polycrystalline InN as previously reported [45]. The obtained values are larger than the recently reported bandgap energy value of pure InN (e. g., 0.7 eV). The possible reasons for the high band-gap value, as mentioned earlier, are the Moss-Burstein (MB) shift, presence of oxygen impurity, and other stoichiometry-related defects [16-21]. The E_g of the films deposited at 100 W is slightly lower than those of 150, 200 and 250 W possibly due to more uniform (less defects) morphology of the InN films grown at 100 W, as deduced from FESEM imaging. The sample deposited at 50 W shows largest bandgap value, e.g., 2.4 eV. This is probably due to very high oxygen content and formation of oxynitride

alloys within the films [46]. In this case, segregated oxygen species could substitute N sites as InO

and form InO_yN_{1-y} alloys resulting in higher bandgap value for films grown at 50 W.

The linear sweep voltammogram (LSV) of InN thin films were recorded in the presence of 0.1

M KOH and the results are shown in **Figure 6**. It can be seen that, after 0 V, the anodic current

increases with increasing an applied bias for all the InN thin films. The bare Si substrate showed

negligible anodic current due to the absence of electro active species on the surface. By increasing of

RF power during the growth of InN thin films from 50 to 200 W, the anodic current decreased then

increased slightly for 250 W. It may be due to a decrease of oxygen content in the InN thin film with

an increase in RF power. This observation is in good agreement with the EDX analysis. The observed

anodic oxidation current is due to the oxygen evolution reaction on the electrode surface in the

presence of KOH [47]. The decrease of oxygen and the increase of nitrogen atomic percentage along

with an increase in RF power lead to a decrease in anodic oxidation current to indicate the corrosion

resistance properties of InN thin films. Furthermore, the onset potential for anodic potentials is slowly

moved to a more positive region by increasing RF Power. Avasarala *et al.* [48] concluded that the

oxidation current of the transition nitrides in the potential range of 1–1.2 V decreases due to the

corrosive resistance behavior of the TiN. Moreover, this study suggests that increasing the nitride

content will lead to decrease in the anodic current due to the increase in corrosion resistance rather

than for oxides and oxynitride based thin films [48]. In the case of InN thin film grown at 250 W

(**Figure 6**), the anodic current was slightly increased due to increases in the oxygen content in the

film, which was already confirmed by EDX analysis (**Figure 4(f)**).

The electrochemical impedance measurements were performed for the InN thin films to investigate the charge transfer dynamics between the InN thin film/electrolyte interfaces during the electrochemical process. Nyquist plots showed that the bare Si substrate showed large semicircle due to very poor conductivity than the InN deposited on Si substrate (**Figure 7(a)**). The semicircle diameter was increased with an increase of RF power from 50 to 200 W and then decreased for 250 W (**Figure 7(b-f)**). The observed semicircle is because of the charge-transfer resistance (R_{ct}) that has taken place at the electrode/electrolyte interface. It is noteworthy that by increasing RF power, the R_{ct} value increases up to 200 W due to decrease of the oxygen content in the InN thin film and this increases the resistivity (**Figure 8**). The EIS data is in good agreement with the LSV results. A decrease in the R_{ct} value leads to an increase in conductivity and the higher anodic current at low RF power used for the growth of InN thin film (**Figure 8**). By increasing the RF power from the 50 to 250 W for the growth of InN thin films, the surface roughness of the films increases and the morphology of the films showed some porous morphology (**Figure 4**). At lower RF power, the particles are interconnected to each other as a result the R_{ct} value decreases. In the case of InN thin film grown at higher RF power, the inter-particle connectivity is not uniform, thus leads to higher R_{ct} value. The difference in the onsets in Re(Z) in the Nyquist plot is due to the presence of various contents of nitrogen in the InN thin film grown at different RF power. It is noted that the interconnection of particles (Refer FESEM images) and content of oxide/nitride phase determine the charge transfer resistance of the InN thin film grown at different RF power.

The Bode phase plots also recorded for the further understanding of charge-transfer resistance of the InN thin films, shown in **Figure 9**. The bare Si substrate showed a broad and indefinite peak in the frequency region of 10 Hz-10 kHz due to the larger charge-transfer resistance at the electrode/electrolyte interface due to a lack of availability for electroactive species. Interestingly, after

11

deposition of InN thin film on the surface of Si substrate a well-resolved peak in the frequency region

of 10 Hz–10 kHz is seen due to a decrease in the charge-transfer resistance. The peaks obtained at

frequencies of 1218, 2036, 2498, 155, and 800 Hz for InN thin films grown at RF powers of 50, 100,

150, 200, and 250 W, respectively. The observed Bode phase angles of 36°, 20°, 28°, 64° and 61° for

InN thin films grown at RF powers 50, 100, 150, 200, and 250 W, respectively. It is noteworthy that

the phase angles, initially decreased, and then increased while increasing RF power and the peaks

shifted to higher frequency regions due to increased nitrogen content in the film. When the phase

angle is greater than or equal to 90°, the electrode behaves like an ideal capacitor and if it is less than

90°, the electrode is permeable to solution ions [49]. In this study, the InN thin film grown at different

RF power supply has the phase angles of less than 90°, which suggests that these thin films can easily

permeate OH⁻ ions.

Electrolyte-based capacitance-voltage measurements were used to evaluate surface charge of

InN thin films grown at different RF power and were recorded by the Mott–Schottky (MS) plots

capacitance method [50-52] as a function of applied potential at a frequency of 1 kHz in 0.1 M KOH

(**Figure 10**). It is clear from the MS plots that all films show negative slopes at a lower bias which

reflects the depletion of the surface accumulation [53, 54]. The donor density and the flat band

potential for the InN thin films can be calculated by using the following Mott–Schottky equation (1)

and (2).

$$\frac{1}{C^2} = \frac{2}{qAN_d\, \varepsilon\varepsilon_0}\, [\, V_{bias} - V_{fb}\, \frac{KT}{q}\,] \qquad (1)$$

$$\text{Slope of}\, (\frac{1}{C^2})\, vs.\, (V_{bias}) = \frac{2}{qAN_d\, \varepsilon\varepsilon_0} \qquad (2)$$

where N_d is the donor density for InN thin films, C is the capacitance of the space charge region, ε is the static dielectric constant of InN, ε_0 is the permittivity of free space, q is elementary electron charge, A is the interfacial area, K is Boltzmann's constant, T is the absolute temperature, V_{bias} is the applied potential, and V_{fb} is the flat band potential. **Figure 10** shows the MS plots obtained for InN thin films. Donor density and flat band potential calculated from MS equations for the InN thin films were plotted as a function of the applied RF power in **Figure 11**. The donor density (N_d) of the InN thin film decreases by increasing the RF power from 50 to 200 W due to the decreasing the oxygen content in the thin film, it is well known that in group III-nitride materials and especially in InN the presence of oxygen in the films raises electron carrier concentration. Oxygen is most common impurity and mostly present at the surface of the nitride films which cause to increase of the carrier concentration. A further increase of RF power to 250 W increases the oxygen concentrations slightly due to the re-sputtering effect. The possible reason is dissociation of InN into In and N atoms due to an increase in surface temperature and thereby oxidation of In surface which causes slight increase of donor concentration. Flat band potential (V_{fb}) values obtained from the MS plots for InN thin film deposited at various RF powers are shown in **Figure 11.** The change in V_{fb} with respect to RF power is due to presence of oxygen which in terns determines the donor concentration at surface causes the band bending at InN thin film/electrolyte interface.

The electrocatalytic behavior of InN thin films grown at various RF power were investigated to elucidate their electron transfer behavior in the presence of $K_3[Fe(CN)_6]$ as a redox couple. The cyclic voltammogram for different InN thin film electrodes were recorded and are shown in **Figure 12(a-f)**. The bare Si substrate did not show any appreciable redox peak current (< 100 nA) in the presence of $K_3[Fe(CN)_6]$ redox couple (**Figure 12(a)**). It is attributed to the lack of availability of the

13

electrocatalytic active materials on the surface of bare Si substrate as a resultant sluggish electron transfer process between the electrode/electrolyte interfaces. But, InN thin films grown at various RF power showed the different electrochemical redox behavior. The InN thin film grown at RF power of 50 W showed the redox current with indistinguishable peaks owing to the high content of In_2O_3 phase present in the thin film (**Figure 12(b)**). Interestingly, reversible and well-defined redox peaks were observed for the InN thin film grown at RF power of 100 W in the presence of Fe(II) /Fe(III) redox couple (**Figure 12(c)**). This is an electrocatalytic behavior of the as grown thin film with the peak-to-peak separation (ΔEp) of 390 mV due to the decreasing the In_2O_3 phase and increasing the InN phase. Moreover, the oxidation and reduction of the Fe^{2+}/Fe^{3+} redox couple with InN thin film prove the enhancement in charge carriers and interfacial transport at the electrode/electrolyte interfaces [13]. By further increasing RF power from 150–250 W for the growth of InN thin films, the reversible voltammetry behavior is disappeared. No obvious oxidation peak was observed during a forward scan with a potential sweep from -1 to +1 V and in contrast, an exponential increase in the cathodic reduction peak current was observed in the reverse scan with potential sweep from +1 to −1 V, starting from 330, 320, and 100 mV and it showed the reduction peaks at 140, -25, and -330 mV for the InN thin films grown at various RF powers of 150, 200, and 250 W, respectively (**Figure 12(d-f)**). The observed shift in the cathodic peak to more negative potential is originated from the increased number of electrons available at the electrode surface for the reduction of Fe(III) to Fe(II). The electrochemical reduction of Fe(III) leads to a decrease in its original concentration during the reverse scan [55]. Hence, the oxidation peak was absent during the forward scan for the InN thin films grown at RF power of 150, 200, and 250 W. This may be due to increasing the InN phase in the thin film with an increase in RF power. The results are in agreement with the XRD patterns.

4. Conclusion

In conclusion, InN thin films were grown by plasma-assisted reactive evaporation on silicon substrate at various RF powers and characterized by suitable analytical techniques. The XRD and micro Raman results show that films were polycrystalline in nature and show a preferential wurtzite structure. The large variation in the band gap measurements has been attributed to the Moss-Burstein (MB) shift and the presence of oxygen. The electrochemical properties of InN thin films were investigated towards water splitting in the presence of 0.1 M KOH. The LSV data revealed the decrease in the anodic current with the increase of nitrogen content in the InN thin films, which results to an increase in corrosion resistance than for oxides and oxynitride based thin films. EIS studies showed increases of R_{ct} value with RF power leads to increase resistivity. Bode phase plots suggest that these thin films can be easily permeable to OH$^-$ ions at InN thin film/electrolyte interface. Change in donor density and flat band potentials with respect to RF power were observed from MS plots. The electrocatalytic response of InN thin films was observed in $K_3[Fe(CN)_6]$ redox probe. The good electrochemical behavior of InN thin films showed that this material could be a potential candidate for water splitting application.

References

[1]   A. Kikuchi, M. Kawai, M. Tada and K. Kishino, *Japan. J.Appl. Phys*, 2004, **43**, L1524–6.

[2]   S. Sakr, E. Warde, M. Tchernycheva, L. Rigutti, N. Isac and F. H. Julien, *Appl. Phys. Lett*, 2011, **99**, 142103.

[3]   J. Wu, *J. Appl. Phy,* 2009, **106**, 011101.

[4]   I. Lo, C.H. Hsieh,Y.C. Hsu,W.Y. Pang and M.C. Chou, *Appl. Phys. Lett*, 2009, **94**, 062105.

[5]   Y. Nanishi, Y. Saito andT. Yamaguchi, *Jpn. J. Appl. Phys*, 2003, **42**, 2549.

[6]   N. U. H. Alvi, P. E. D. S. Rodriguez and V. J. Go´mez, *Appl. Phys. Express,* 2013, **6,** 115201.

[7]   SJ. Pearton, BS. Kang, S. Kim, F. Ren, BP. Gila, CR. Abernathy, Jenshan Lin, and S N G Chu, *J Phys: Condens Mat,* 2004, **16**, R961.

[8]   N. Sofikiti, N. Chaniotakis, J. Grandal , M. Utrera, M.A. Sánchez-García and E. Calleja, *Mater. Lett,* 2010, **64,** 1332.

[9]   H. Lu, W. J. Schaff, and L. F. Eastman, *J. Appl. Phys*, 2004, **96**, 3577.

[10]   N. Chaniotakis and N. Sofikiti, *Anal. Chim. Acta*, 2008, **615**, 1.

[11]   B AlOtaibi, M Harati, S Fan, S Zhao, H P T Nguyen, M G Kibria and Z Mi, N*anotechnology* 2013, **24**, 175401.

[12]   S. H. Kim, M. Ebaid, J-H. Kang and S-W. Ryu, *Appl. Surf. Sci., 2014,* **305**, 638.

[13]   J. Wallys, S. Hoffamann, F. Furtmayr, J. Tebuert and Eickhoff, *Nanotechnology*, 2012, **23**,165701.

[14]   S-W. Ryu, Y. Zhang, B. Leung, C.Yerino and J. Han, *Semicond. Sci. Techno,* 2012, **27,** 015014.

[15]   V.Y. Davydov, A.A. Klochikhin, R.P. Seisyan, V.V. Emtsev, S.V. Ivanow, F. Bechstedt, J. Furthmuller, H. Harima, A.V. Mudryi, J. Aderhold, O. Semchinova and J. Graul, *Phys. Status Solidi B*,2002, **229,** r1.

[16]   J. Wu, W. Walukiewicz, S.X. Li, R. Armitage, J.C. Ho, E.R. Weber, E.E. Haller, H. Lu,

W.J. Schaff, A. Barcz and R. Jakiela, *Appl. Phys. Lett*, 2004, **84**, 2805.

[17] T. Matsuoka, H. Okamoto, H. Takahata, T. Mitate, S. Mizuno, Y. Uchiyama and T. Makimoto, *J. Cryst. Growth*, 2004, **269,** 139.

[18] M. Yoshimoto, H. Yamamoto, W. Huang, H. Harima, J. Saraie, A. Chayahara and Y. Horino, *Appl. Phys. Lett*, 2003, **83,** 3480.

[19] J.J. Kim, E. Ikenaga, M. Kobata, A. Takeuchi, M. Awaji, H. Makino, P.P. Chen, A. Yamamoto, T. Matsuoka, D. Miwa, Y. Nishino, T. Yamamoto, T. Yao and K. Kobayashi, *Appl. Surf. Sci*, 2006, **252,** 5602.

[20] T.V. Shubina, S.V. Ivanov, V.N. Jmerik, D.D. Solnyshkov, V.A. Vekshin, P.S. Kop'ev, A. Vasson, J. Leymarie, A. Kavokin, H. Amano, K. Shimono, A. Kasic and B.Monemar, *Phys. Rev. Lett*, 2004, **92**, 117407.

[21] K.S.A. Butcher, M.W. Fouquet, P.P.T. Chen, T.L. Tansley, H. Dou, S.K. Shrestha, H. Timmers, M. Kuball, K.E. Prince and J.E. Brad, *J. Appl. Phys*, 2004, **95**, 6124.

[22] J. Y. Kim, G. Magesh, D. H. Youn, J.-W. Jang, J. Kubota, K. Domen and J. S. Lee, *Sci. Rep.*, 2013, **3**, 2681

[23] N. u. H. Alvi, P. E. D. S. Rodriguez and V. J. Go´mez, *Appl. Phys. Express* 2013, **6**, 115201.

[24] B. Zhang, H. Song, J. Wang, C. Jia, J. Liu, X. Xu, X. Liu, S. Yang, Q. Zhu, Z. Wang, *J. Cryst. Growth*, 2011, **319**, 114.

[25] R. Ohba, K.Mitamura, K.Shimomoto, T.Fujii, S.Kawano, J.Ohta, H.Fujioka,, M.Oshima, *J. Cryst. Growth*, 2009, **311**, 3130.

[26] X.M. Cai, F.Ye, Y.Q. Hao, D.P. Zhang, Z.H. Zhang and P. Fan, *J. Alloy compd.*, 2009, **484,** 677.

[27] A. L. Syrkin, V. Ivantsov, A. Usikov, V. A. Dmitriev, G. Chambard, P. Ruterana, and A. V. Davydov, *phys. stat. sol. (c)*, 2008, **5**, 1792.

[28] K. Sumitani, R. Ohtani, T. Yoshida, Y. Nakagawa, S. Mohri, T. Yoshitake, *Diamond Relat. Mater.*, 2010, **19**, 618.

[29] M. Alizadeh, H. Mehdipour ,V. Ganesh, A. N. Ameera, B. T. Goh, A. Shuhaimi, S. A. Rahman, *Appl. Phys. A*, 2014, **117**, 2217.

[30] M. V. S. da Silva, D. G. F. David, I. Pepe, and A. Ferreira da Silva, *Thin Solid films*, 2012, **520**, 4848.

[31] M. Jamil, H. Zhao, J. B. Higgins, and N. Tansu, *phys. stat. sol. (a)*, 2008, **205**, 2886.

[32] T.-T.Kang, X. Liu, R. Q. Zhang, W. G. Hu, G. Cong, F.-A. Zhao, and Q. Zhu, *Appl. Phys. Lett*, 2006, **89**, 071113.

[33] H. Cheng, Y. Sun, J.X. Zhang, Y.B. Zhang, S. Yuan, and P. Hing, *J. Cryst. Growth*, 2003, **254**, 46.

[34] T. F. G. Muller, D. Knoesen, C. Arendse, R. Swanepoel, and S. Halindintwali, C. Theron, *Thin Solid Films*, 2006, **501**, 98.

[35] M. Alizadeh, H. Mehdipour, B.T. Goh and S.A. Rahman, *J. Appl.* Phys, 2013, **114**, 024301.

[36] M. Jothibas, C. Manoharan, S. Ramalingam, S. Dhanapandian, S. Johnson Jeyakumar, M. Bououdina, *J. Mol. Struct.*, 2013, **1049**, 239.

[37] K.P. Biju and Mahaveer K. Jain *Appl.Surf. Sci,* 2008, **254**, 7259.

[38] X.-M. Cai, ,F. Ye, Y.-Q. Hao, D.-P. Zhang, Z.-H. Zhang and P. Fan *J. Aloyl. Compd* 2009, **484**, 677.

[39] B. Song, J.K.Jain, G. Wang, Z.H.Zhang, M. lei, H.Q.Bao and X.L.Chen, *Physica E*, 2008, **40**, 579.

[40] T. Inushima, T. Shiraishi, and V. Yu. Davydov, *Solid State Commun*. 1999, **110**, 491.

[41] M-C. Lee, H-C. Lin, Y-C. Pan, C-K. Shu, J. Ou, W-H. Chen, and W-K Chen, *Appl.Phys.Lett*, 1999, **73**, 2606.

[42] Y. Chen, X. Zhou, X. Zhao, X. He, X. Gu, *Mat. Sci. Eng. B-Solid,* 2008, **151** 179.

[43] S. Kumar, L. Mo, T.L. Motlan and T.L. Tansley, *Jpn. J. Appl. Phys*, 1996, **35**, 2261.

[44] K.P. Biju, M.K. Jain**, *Appl. Surf. Sci.*, 2008, **254**, 7259.

[45] K.S.A. Butcher, T.L. Tansley, *Superlattices Microstruct.,* 2005, **38**, 1.

[46] D. Alexandrov, K.S.A. Butcher, M. Wintrebert-Fouquet, *J. Cryst. Growth*, 2004, **269**, 77.

[47] S. Chen and S. Z. Qiao, *ACS Nano*, 2013, **7**, 10190.

[48] B. Avasarala and P. Haldar, *Electrochim. Acta*, 2010, **55**, 9024.

[49] F. Matemadombo and T. Nyokong, *Electrochim. Acta*, 2007, **52**, 6856.

[50] R. Shinar and J. H. Kennedy *Solar. Energ. Mater.*, 1982, **6**, 323

[51] T. Schubert, G. Steinhoff, H.-G. von Ribbeck, M. Stutzmannn, M. Eickhoff, and M. Tanaka, *Eur. Phys. J. E* 2009, **30**, 233.

[52] D. Chauhan, V R Satsangi, S. Dass and R. Shrivastav *B. Mater. Sci*, 2006, **29**, 709.

[53] J. W. Ager III , N. Miller, R. E. Jones, K. M. Yu, J. Wu, W. J. Schaff and W. Walukiewicz *phys. stat. sol. (b)*, 2008, **245**, 873.

[54] J. W. Ager III , R. E. Jones, D. M. Yamaguchi, K. M. Yu, W. Walukiewicz, S. X. Li, E. E. Haller, H. Lu and W.J.Schaff *phys. stat. sol. (b)*, 2007, **244**, 1820.

[55] G. Steinhoff, *Group III-Nitrides for Bio- and Electrochemical Sensors*, Ph.D thesis, 2008, **Chapter 5.3**, Page: 103

Table

Table 1. The thickness and bandgap energy values of InN films deposited at various RF powers.

RF power (W)	Thickness (nm)	Bandgap energy (eV)
50	840	2.4
100	710	1.8
150	650	2.0
200	630	2.0
250	580	1.95

Figures and Caption
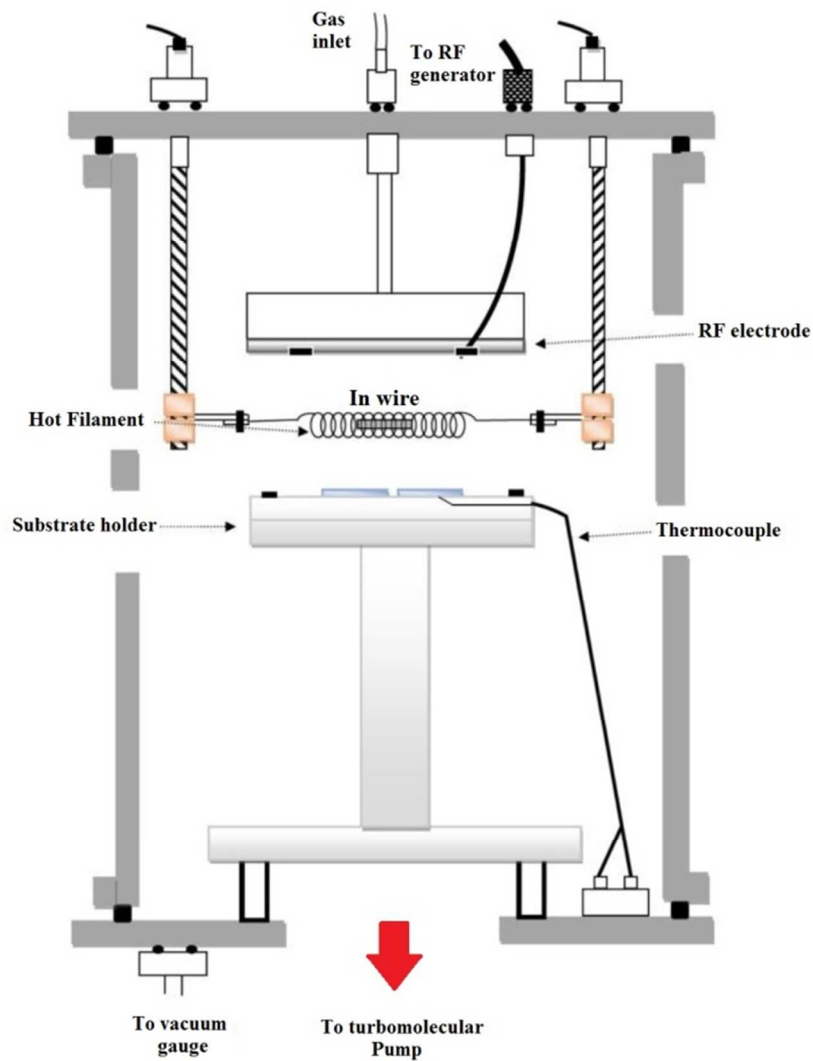
Figure 1. The schematic diagram of plasma-assisted reactive evaporation system.
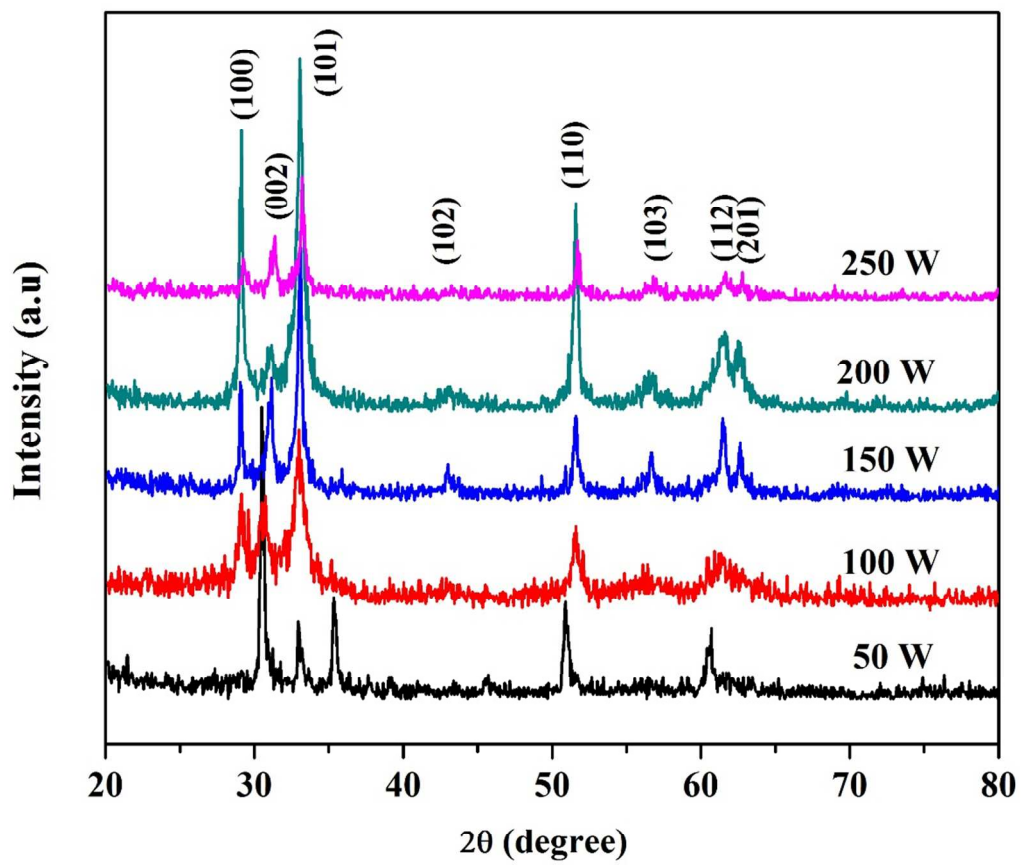
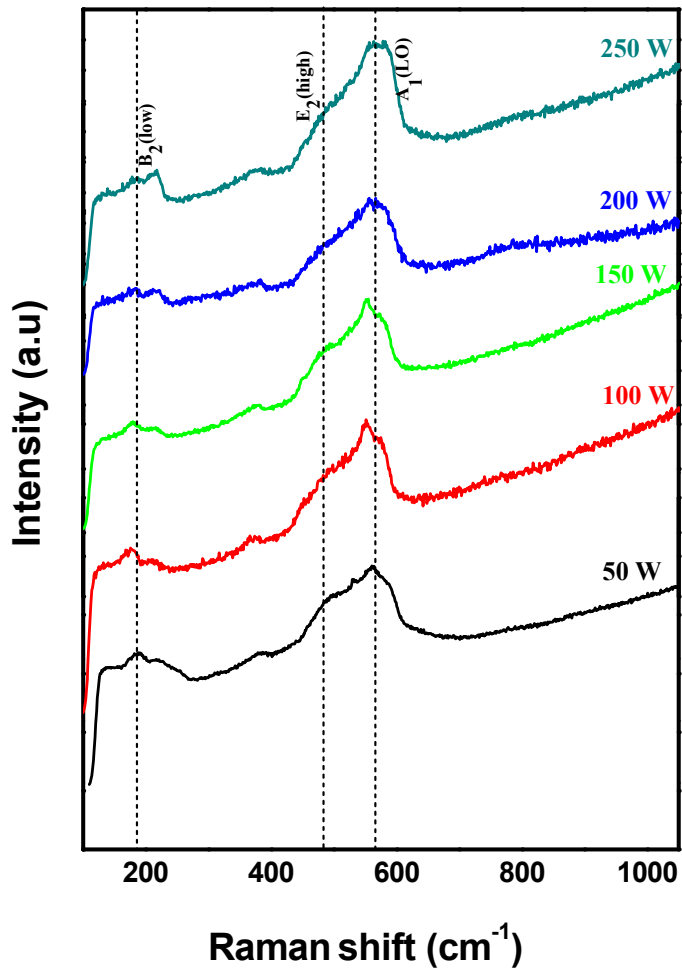**Figure 2**. X-ray diffraction patterns of the InN thin films grown at different applied RF powers.

Figure 3. Micro Raman spectra of the InN thin films deposited at different applied RF powers.
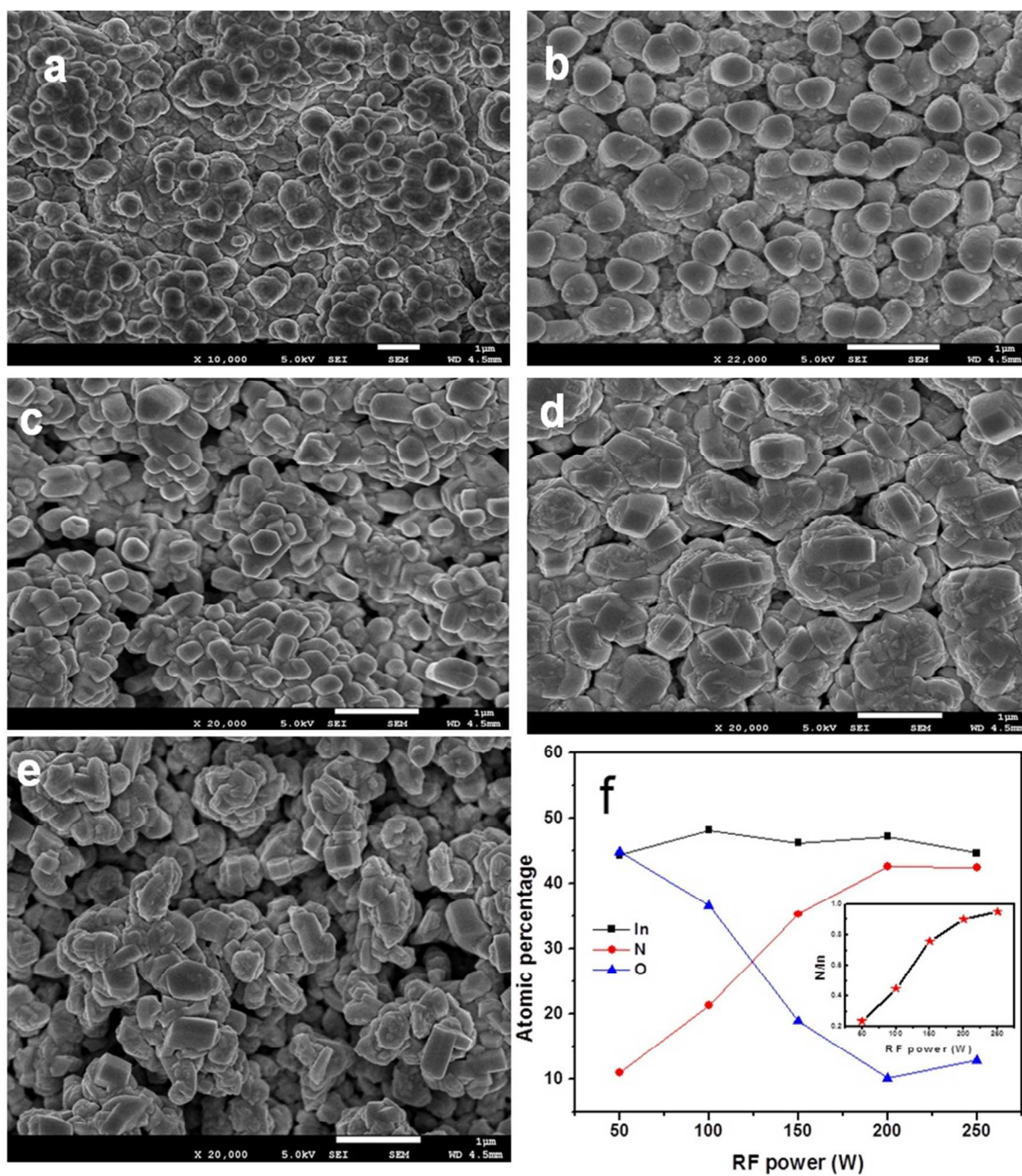
Figure 4. FESEM images of the InN thin films grown at the applied RF powers of 50 W (a), 100 W (b), 150 W (c), 200 W (d) and 250 W(e); Dependence of the elemental percentage of the InN films on the applied RF power (f).
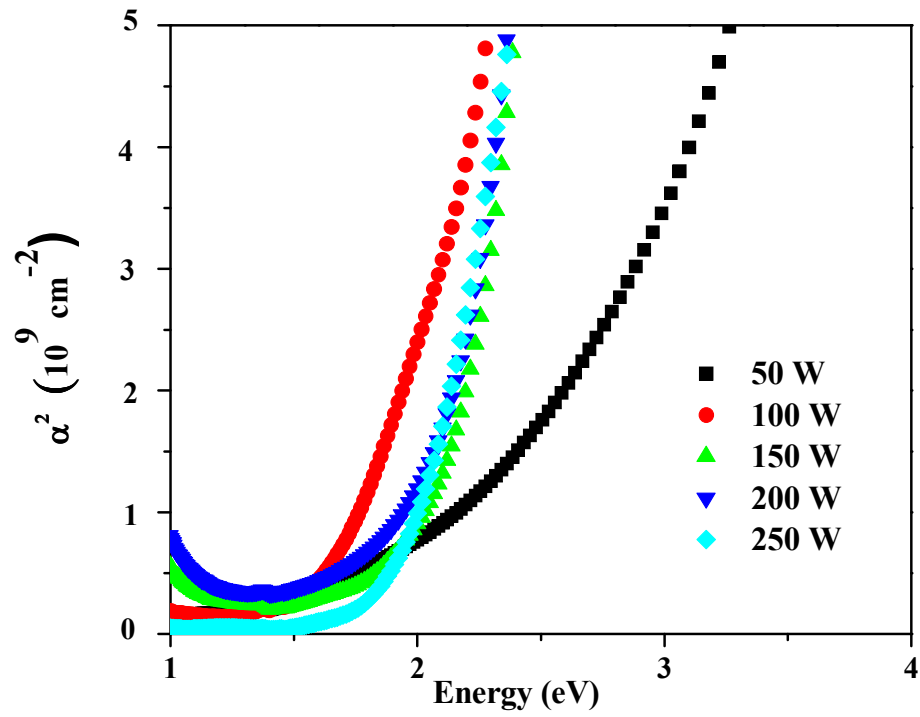
Figure 5. Plots of α^2 versus $h\upsilon$ for the InN thin films grown at various applied RF powers.
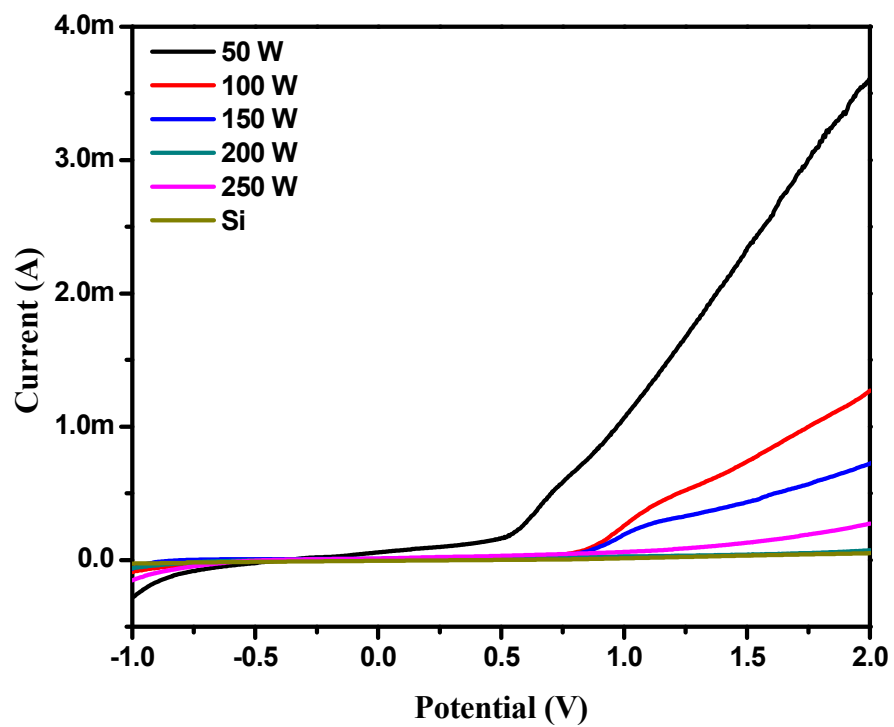
Figure 6. Linear sweep voltammograms of the InN thin films grown at different applied RF powers.
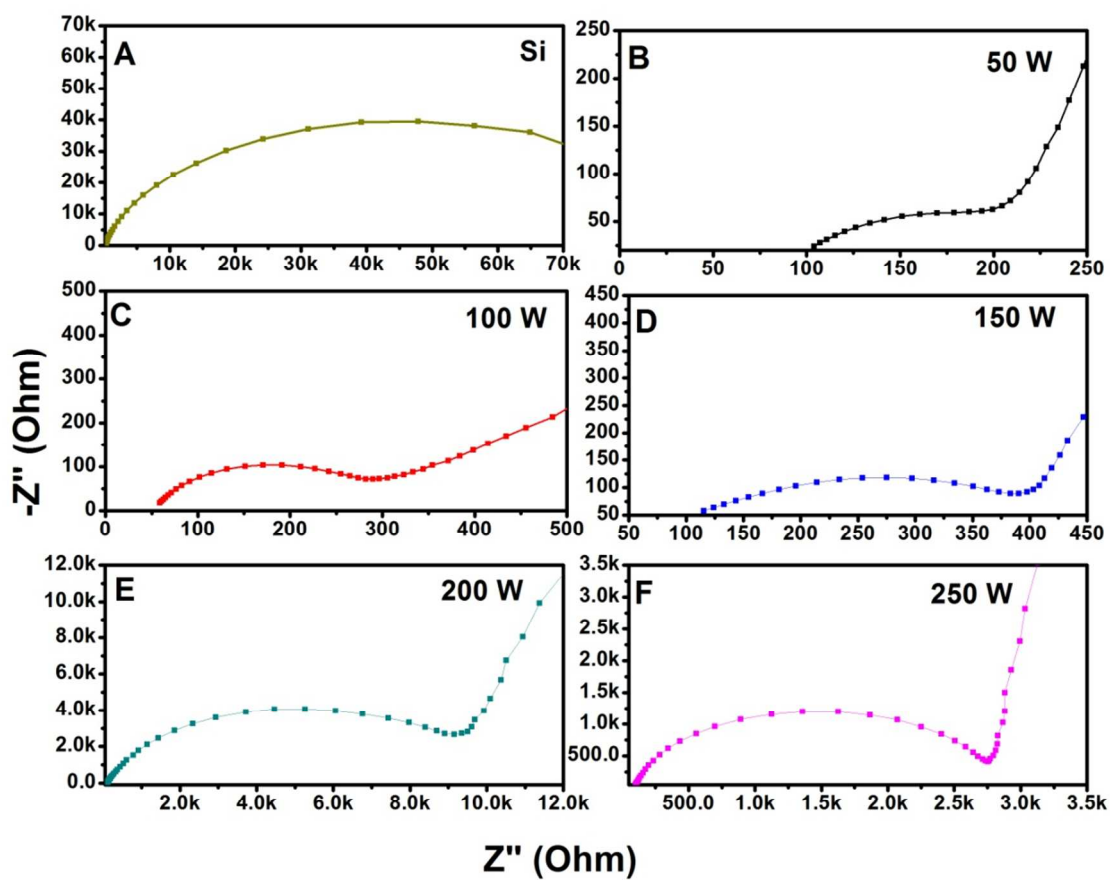
Figure 7. Nyquist plots of the Si substrate (a) and the InN thin films deposited at the RF powers of 50 W (b), 100 W (c), 150 W (d), 200 W (e) and 250 W (f).
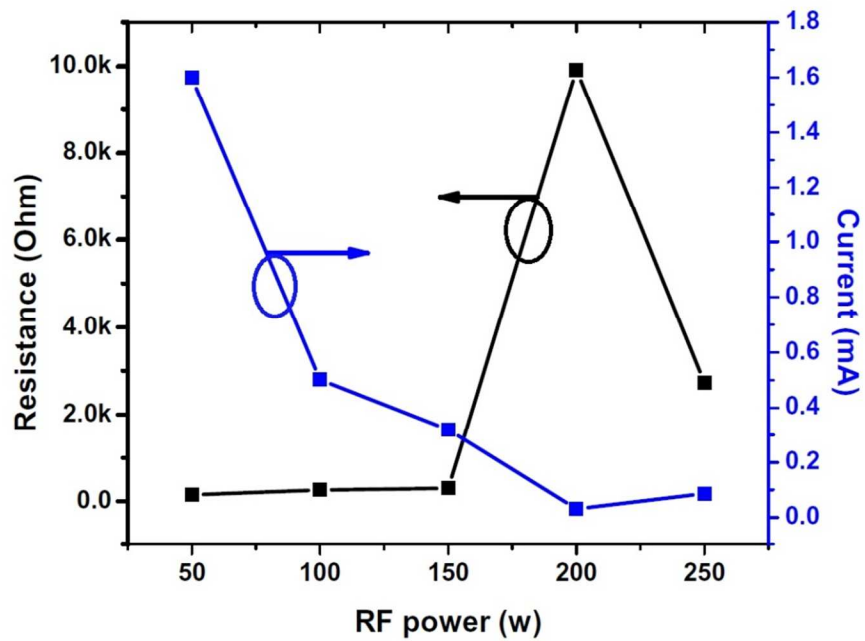
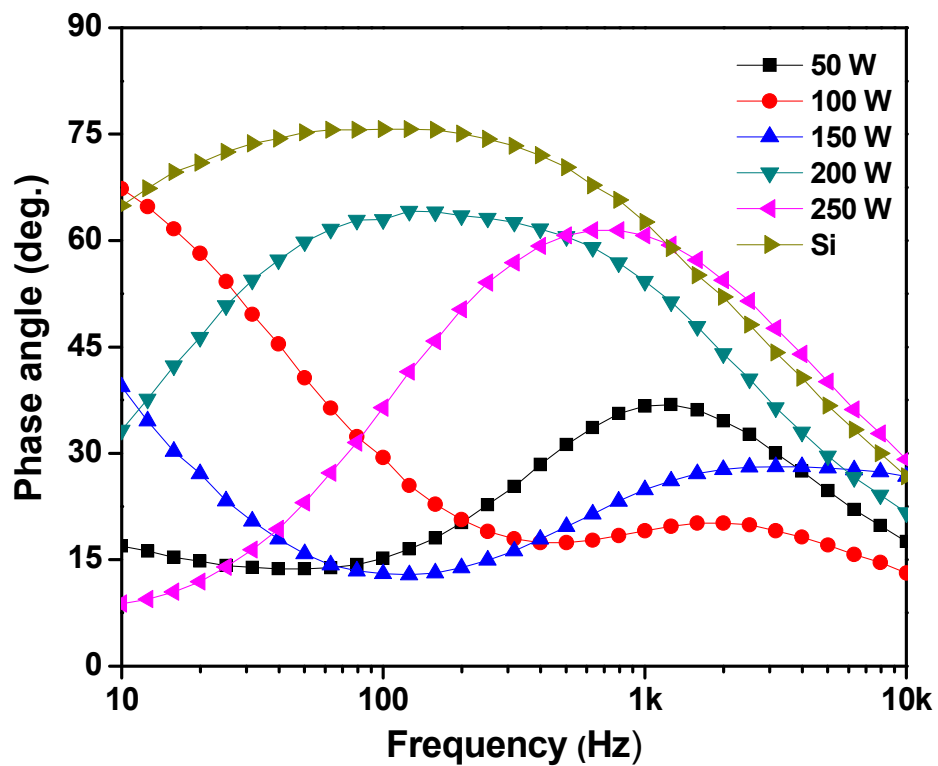**Figure 8**. Dependence of current and resistance of the InN thin films on the applied RF powers.

Figure 9: Bode angle phase plots of the InN thin films grown at different RF power in the presence of 0.1 M KOH.
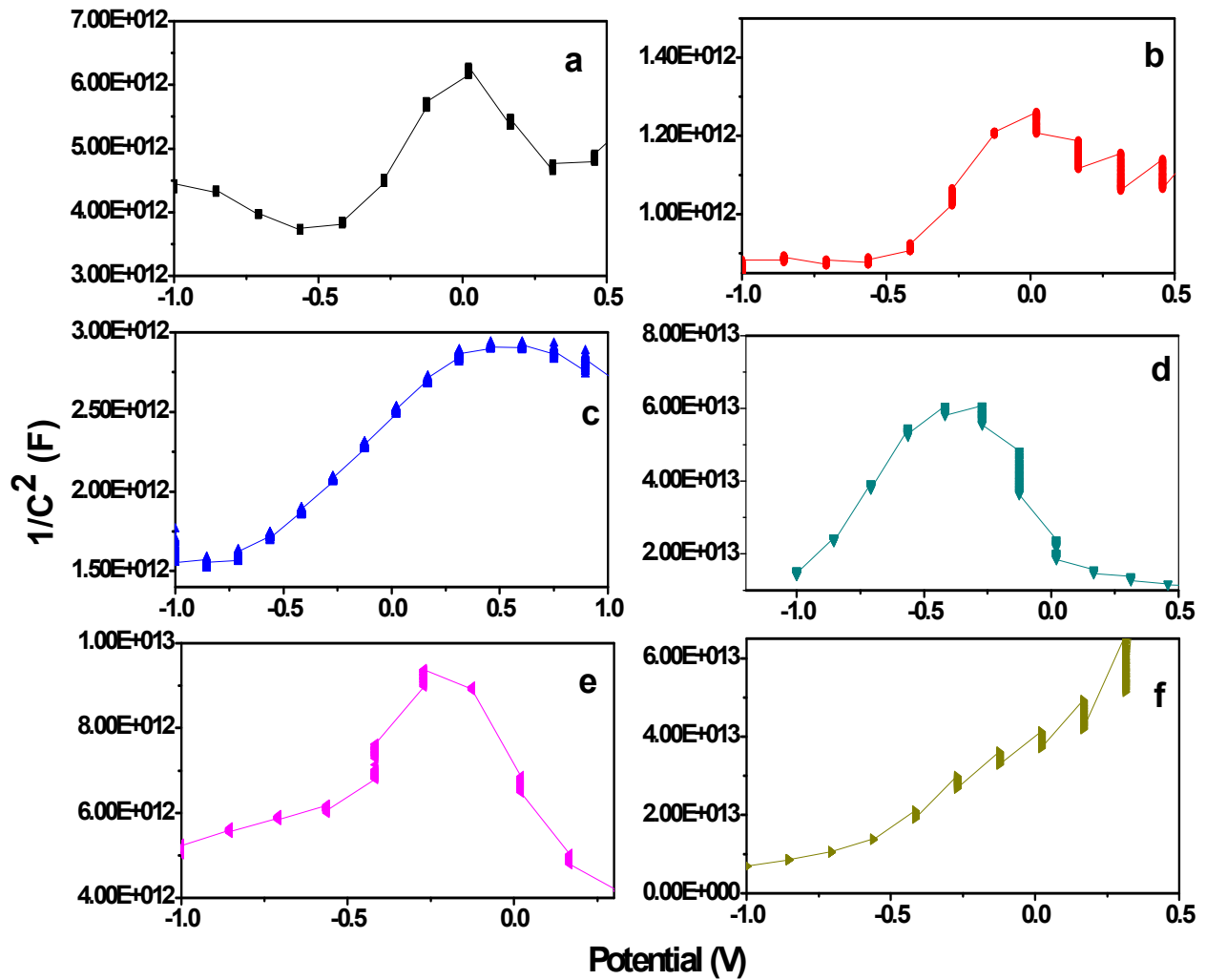
Figure 10. Mott–Schottky plots of the measured capacitance of the Si substrate (a) and the InN thin films grown at RF powers of 50 W (b), 100 W (c), 150 W (d), 200 W (e) and 250 W (f).
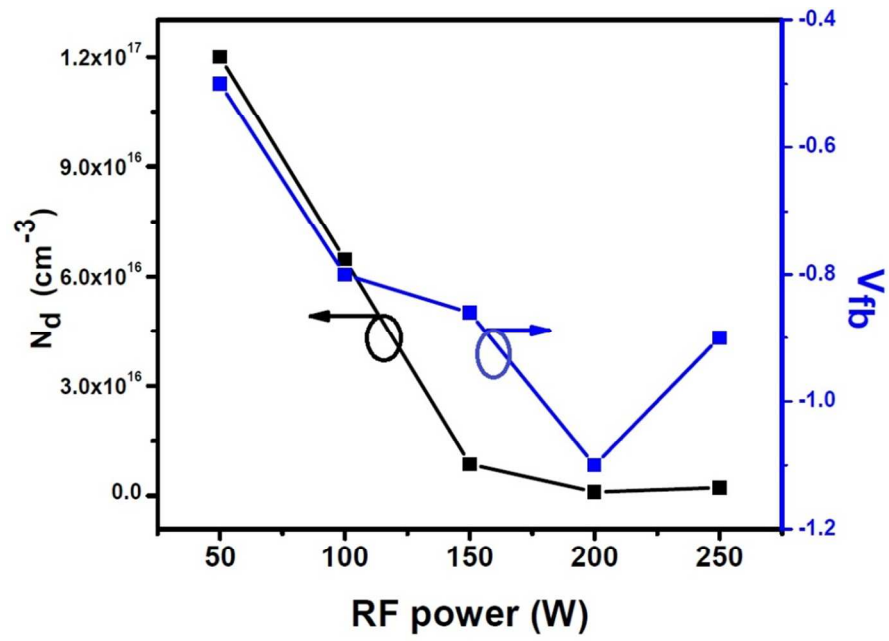
Figure 11. Dependence of donor density and flat band potential of the InN thin films on the applied RF power.
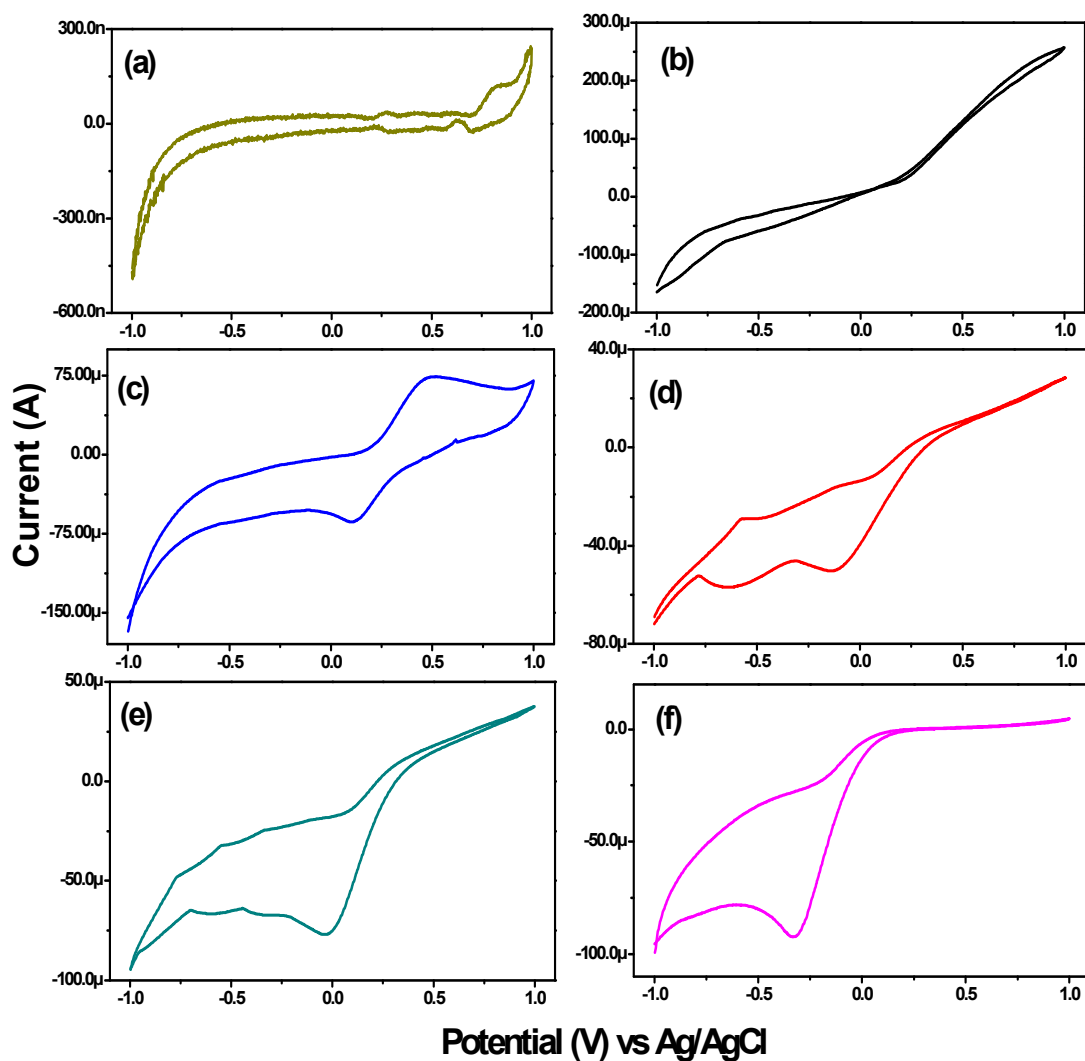
Figure 12. Cyclic voltammograms of the Si substrate (a) and the InN thin films grown at the applied RF powers of 50 W (b), 100 W (c), 150 W (d), 200 W (e) and 250 W (f) in the presence of 1 mM $K_3[Fe(CN)_6]$ and 0.1 M KCl solution at a scan rate of 50 mV/s.

32